Journal of
Nanomedicine & Nanotechnology

Basuray et al., J Nanomed Nanotechnol 2015, 6:3
DOI: 10.4172/2157-7439.1000293

Research Article Open Access

Single Molecule Oscillations of an RNA/DNA Duplex in a Plasmonic Nanocavity

Sagnik Basuray[1†], Avinash Pathak[1†], Biyan Chen[1], Drew Menke[2], Charles M Darr[3], Keshab Gangopadhyay[1,4], Peter V Cornish[2*] and Shubhra Gangopadhyay[1*]

[1]*Department of Electrical and Computer Engineering, 349 Engineering Building West, University of Missouri, Columbia, MO 65211, USA*
[2]*Department of Biochemistry, 117 Schweitzer Hall, University of Missouri, Columbia, MO 65211, USA*
[3]*Department of Bioengineering, 349 Engineering Building West, University of Missouri, Columbia, MO 65211, USA*

Abstract

We report the visualization of single molecule dynamics in epifluorescence mode through extraordinary plasmonic enhancement provided by silver grating with embedded nanocavities. Cy3/Cy5-labeled DNA/RNA hybrid duplexes were affixed to SiO_2-capped silver gratings produced by soft lithography process. Tracking single-molecule fluorescence revealed damped sub-1 Hz periodic Cy3 intensity fluctuations with strong dependence on the bulk $MgCl_2$ concentration. Extreme concentration of electric field at the nanocavity edge induces plasmonic heating, which sets up convection deep within the nanocavity. Local fluctuations in Mg^{2+} ion concentration promote a bent or unbent duplex conformational state, respectively, by varying degrees of negative charge screening along the duplex backbone. These oscillations continue until the duplex conformational state stabilizes or the dyes bleach. This unique molecular behavior in the nanocavity could be used to study duplex complementarity, structural polymorphisms, and protein-nucleic acid interactions at the single molecule level.

Keywords: Plasmonics; Silver; Gratings; RNA/DNA duplex; Single-molecule fluorescence; Epifluorescence; Oscillation

Introduction

Single-molecule (SM) analytical techniques have proven capable of revealing elusive biomolecular interaction fundamentals critical to advancing our knowledge of complex cellular pathways, mechanisms of disease pathogenesis, and next-generation translational research in novel drug design [1-4]. SM studies monitor the stochastic behavior of individual biomolecules under specific experimental conditions (e.g. temperature, salt concentration, enzyme substrates, analytes of interest, etc.) through the lens of a high-fidelity reporter (e.g. fluorescence). Elucidation of SM dynamics by fluorescence requires experimental setups that isolate individual molecules and simultaneously overcome the poor intrinsic signal-to-noise ratio (SNR) of single fluorophore labels over background. Using quartz as the immobilization substrate mitigates glass auto fluorescence, but epifluorescence microscopes introduce additional noise through excitation of the bulk solution. This is most often addressed through the use of complex optical setups such as total internal reflection (TIR) microscopes [5-7]. Alternatively, SM fluorescence and SNR can be improved through resonant photon coupling to surface plasmon polaritons extant at a metal-dielectric interface (SPR) [8]. SPR coupling to plasmonic active metals (e.g. gold, silver) generates a highly-concentrated evanescent electric (E-) field that is typically several-fold higher magnitude than the incident field, significantly increasing excitation rate as well as radiative decay rate of fluorophores immobilized near the plasmonic surface with respect to a quartz surface [9-11].

Matching the optical momentum of incident light to the propagation constant of the surface plasmons is difficult to achieve with flat metal films except through the use of high index prisms, but may be realized in free space by introducing wavelength-scale periodic perturbations on the metal-dielectric interface (i.e. gratings) [12-14]. Plasmonic E-field enhancement can also be produced locally (LSPR) by concentrating coupled light using nanostructured surface morphologies with geometric singularities such as bowties/nanoantennae, [15,16]. nanolenses, [17] tip resonators, [18] and nanohole arrays [19]. Integrating LSPR light concentration through nanoscale geometric singularities with SPR coupling substrates leads to size-tunable, additive field enhancement and concentration [20-22]. Such enhancement may be sufficient to permit visualization of single molecules using less expensive and complex epifluorescence optical setups.

In this work, we have used a nanoscale periodic metallic grating with embedded nanocavities fabricated by a cost-efficient soft lithography process to achieve fluorescence enhancement factors sufficient to visualize single molecule dynamics in an epifluorescence microscope. The plasmonic substrate takes advantage of the strong free space light coupling properties of silver SPR gratings and field concentration at the discontinuities in the metal provided by the randomly generated 20-200 nm nanocavities, which we have previously shown to provide fluorophore enhancement exceeding 100-fold with respect to glass [14]. We demonstrate the single molecule fluorescence capabilities of this system using a fluorophore-pair-labeled RNA/DNA hybrid duplex. Moreover, we report a unique observation that those duplex molecules identified as residing deep within the nanocavities exhibit ion-concentration-dependent conformational rearrangements in the form of fluorescence intensity oscillations. This behavior is related back to the duplex structure, nanocavity dimension, and significant charge screening set up by the high ionic strength in the nanocavity. We

***Corresponding author:** Shubhra Gangopadhyay, 141A Engineering Building West, University of Missouri, Columbia, MO 65211-2300, USA, Tel: 1-573-882-4070; Fax: 1-573-884-0312; E-mail: gangopadhyays@missouri.edu

Peter V Cornish, 117 Schweitzer Hall, University of Missouri, Columbia, MO 65211, USA, Tel: 1-573-882-0443; Fax: 1-573-882-5635; E-mail: cornishp@missouri.edu

Received April 06, 2015; **Accepted** May 05, 2015; **Published** May 15, 2015

Citation: Basuray S, Pathak A, Chen B, Menke D, Darr CM, et al. (2015) Single Molecule Oscillations of an RNA/DNA Duplex in a Plasmonic Nanocavity. J Nanomed Nanotechnol 6: 293. doi:10.4172/2157-7439.1000293

anticipate this observation could be extended to identify polymorphisms or duplex-target interactions through frequency modulation at a specific ion concentration.

Materials and Methods

Sample preparation for single molecule experiments

Silver gratings were fabricated on silicon substrates using a soft lithography stamping process replicating an HD DVD grating mold as described previously [14]. Briefly, poly-(methylsilsesquioxane) (PMSSQ, GR650F, Techneglas) was stamped onto a cleaned silicon wafer followed by sputter deposition of a 2 nm titanium adhesion layer and 100 nm silver layer. Mechanical stresses incurred in the stamping process result in formation of randomly sized and distributed nanocavities. A 10 nm SiO_2 capping layer was then deposited by e-beam physical vapor deposition.

Cy3/Cy5 dye pair-labeled DNA-RNA (duplex) hybrid molecules were immobilized on both SiO_2-capped silver gratings with embedded nanocavities and unmodified glass coverslips for comparison. A 50 µL aliquot of 1× T50 buffer solution (10 mM TRIS, 50 mM NaCl, pH 8.0) was first dispensed on the substrate surfaces followed by 10 min incubation with an additional 50 µL of 1 µg/µL biotinylated bovine serum albumin (BSA-Biotin) in T50 buffer. Excess BSA-Biotin was removed by rinsing with 50 µL fresh T50 buffer. Neutravidin (50 µL) was then added and incubated for 5 minutes followed by another T50 buffer rinse. Finally, the duplex molecules were dispensed on the surface in imaging buffer (20 µL 5× T50 buffer, 15 µL 2 M MgCl, 1.6 µL D-Glucose, 1 µL Gloxy, and 74.2 µL Trolox) to avoid fluorophore blinking.

SiO_2-capped silver grating platforms were cleaned using high-pressure nitrogen flow just prior to flow cell fabrication. Solvent-based washing was avoided to prevent damage to the silver or underlying PMSSQ layer. The flow cell was constructed by drilling entry and exit holes through a glass or quartz slide using a Dremel tool with a 0.75 mm diamond-coated bit. Glass spacers were secured at the edges by 5-minute epoxy (Devcon Home) and the grating was secured between the entry/exit holes. Slides and coverslips were cleaned by high-pressure N_2 flow, passed over a diffuse flame, and allowed to cool. Double-sided tape was then used to separate each set of holes and define the ends and the cell was capped by a N_2-cleaned coverslip. Finally, the ends were closed using a 5-minute epoxy.

Instrumentation and measurement details

Single molecule fluorescence measurements were performed on an Olympus IX-71 inverted microscope with custom epifluorescence excitation setup. Excitation sources were 100 mW 532 nm or 642 nm diode-pumped solid-state lasers (Spectra Physics, Excelsior One) to monitor Cy3/Cy5 FRET or only Cy5 emission, respectively. Laser power was attenuated to appropriate fluence (4.6 mW) by a 532 nm or 633 nm zero-order half-wave plate (Thor Labs, WPH05M-532/-633), respectively, and neutral density filters (ThorLabs, NE40B, NE30B, NE20B, NE10B, NE06B, NE05B, NE04B, NE03B, and NE02B). Fluorophore emission was collected using either an UPlanSApo 100× oil-immersion objective (Olympus, NA=1.40) or UPlanSApo 60× water-immersion objective (Olympus, NA=1.20) using a zt532rdc dichroic and HQ545lp long-pass filter (Chroma) with additional 630dcxr dichroic/shot-pass filter to separate Cy3 and Cy5 emission into individual channels. Fluorescence intensities were recorded on an Andor iXon$^+$ EMCCD camera at a rate of 10 frames per second (fps) for a total length of 1200 frames and 100 ms integration time per frame. Camera gain and scaling factors were kept constant for all substrates to allow for direct comparison of intensity values, signal-to-noise ratio, and calculation of fluorescence enhancement factors.

Fluorescence recording analysis

Fluorescence recordings were analyzed by MATLAB® for single-molecule fluorescence intensity and power spectral density (PSD) of the intensity-time plots. Considering the low (pM) concentration of duplex added to the substrates, molecules are assumed to be sufficiently isolated so that intensity above the background noise represent individual molecules. Pixel intensities above the average first-frame intensity were recorded and analyzed across all frames as potential single-molecule fluorophores while below-average values are ignored. Presence of solitary dye-labeled duplex molecules was confirmed by identification of a single-step photobleaching event. FRET efficiency was analyzed by evaluating relative pixel intensity in both the donor and acceptor emission channel. Correct pixel mapping was confirmed daily prior to any experiment by running a plain glass slide with immobilized red fluorescent beads.

PSD calculation was performed using a Fast Fourier Transform (FFT) on the entire frameset from a fluorescence recording (1200 frames per 2 min recording). The Nyquist criterion [23]. gives a maximum recordable frequency of 5 Hz. Once a FFT command was executed on each trace file, the conjugate of the resultant FFT value was multiplied by the FFT values to derive the ultimate power contained within each frequency. This was then plotted with frequencies from 0 to 5 Hz along the x-axis. Pre- and post-photobleaching regions were isolated with the post-photobleaching region then representing the background for calculating enhancement and PSD.

Results

Plasmonic-enhanced single molecule Förster resonance energy transfer (smFRET) studies were performed using an RNA-DNA hybrid structure hereafter referred to as 'duplex' (Figure 1A) affixed to our SiO_2-capped silver plasmonic gratings with embedded nanocavities (Figure 1B) [14]. The duplex consists of a 137-base RNA backbone with 29-bp biotinylated DNA tethered to the substrate, 11-base open RNA region, 20-bp DNA labeled with Cyanine 3 (Cy3) donor and Cyanine 5 (Cy5) acceptor at opposite ends, and 77-base RNA tail extending into the medium. The 6.8 nm (20-bp) Cy3-Cy5 dye separation provides only ~20% FRET efficiency given the nominal Förster distance R_o=5.4 nm, [24]. so that the Cy3 donor fluorescence typically dominates under normal circumstances. The conformal 10 nm SiO_2 acts as a spacer layer to prevent metal-based fluorescence quenching, mitigate silver degradation in the aqueous environment, and provide a hydroxyl-terminated (-OH) surface to promote adsorption of biotinylated BSA. Biotin-streptavidin linkage immobilizes the duplex to the surface, providing a Cy3-dominated fluorescence intensity map visible in epifluorescence mode (Figure 1C). As can be seen in Figure 1C, there is a distribution of fluorescence intensities across the surface with highest intensity located along the grating-nanocavity interface. These were confirmed to be single molecules by the presence of single-step photobleaching, indicating the intensity distribution was due to some variation in the enhancement of individual fluorophores across the substrate.

The plasmonic nanocavities result from shear stresses incurred in the stamp and polymer ink during fabrication and range in size from 20-200 nm in width and 20-100 nm in depth, intersecting the grating in randomly distributed and oriented arrangements [14]. Quantitation

of the morphology-mediated plasmonic-enhanced E-field strength is fundamental to understanding the associated fluorescence enhancement phenomena. Figure 1D shows an electric field distribution at the cross-section of gratings with a 50 nm wide and 100 nm deep vertical nanocavity by finite-difference time-domain (FDTD) simulation (details in Supplementary Section 1 (Figures S1-S6)) [14]. For the simulation, the plasmonic substrate was illuminated using 532 nm light at the associated resonance angle given by the dispersion relation for 400 nm grating spacing (θ_{SP}=8°). Figure 1D shows E-field enhancement ($E_z/E_{z,0}$) of as much as 19× the incident field strength where the propagating surface plasmon polaritons (SPPs) are concentrated at the upper edge of the grating intersection with the nanocavity. Meanwhile, the water-filled depths within the nanocavity experience much lower E-fields due to field concentration at the geometrical singularity of the nanocavity edge. E-field magnitude increases with increasing height through the nanocavity edge from ~1× up to 2.5× the incident field strength in the area just above the nanocavity as shown by the field intensity profile (Figure 1E) of the middle of the nanocavity (the white dashed line in Figure 1D).

Figure 2 shows smFRET time traces extracted from multiple SM fluorescence movies recording intensity dynamics across a range of $MgCl_2$ concentrations from 10 mM to 1 M. Duplex mounted on quartz (Figure 2A) or on plasmonic grating surface away from the nanocavities (Figure 2B) exhibit no anticorrelated FRET behavior or intensity fluctuation observable above the noise prior to single-step photobleaching. Such behavior was expected as the dyes were separated to the lower limit of FRET efficiency. However, analysis of the molecules localized in the nanocavities such as those in Figure 2C displayed sub-1 Hz fluorescence intensity oscillations, especially at extremely high $MgCl_2$ concentrations (Figures 2D - 2F). Statistical analysis showed that these oscillations were not unique to only a few molecules, but seen in more than 50% of duplex single molecules immobilized within nanocavities (Supplementary Figure S7). It is important to note that Cy3 intensity oscillations occurring for dyes in the nanocavities (Figure 2D) were recorded in the same movies as non-fluctuating dyes outside the nanocavities (Figure 2B), which suggests there is a unique property

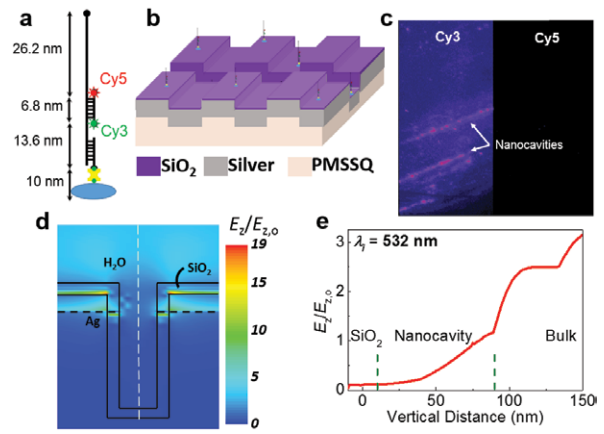

Figure 1: (A) Structure of the dye-labeled RNA/DNA duplex; (B) Schematic of the grating with embedded nanocavity; (C) Representative frames from the split-channel Cy3/Cy5 FRET recordings; (D) Simulated electric field distribution at the nanocavity-grating interface (black dashed line indicates the level of the base of the grating); and (E) Electric field depth profile along the middle of the nanocavity (white dashed line in (D))

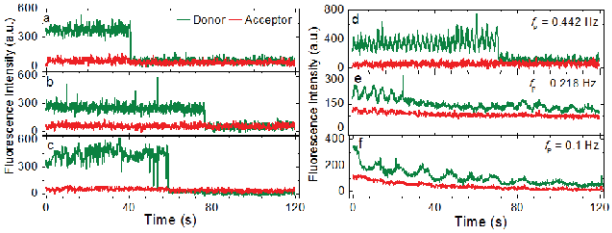

Figure 2: (A and B) Cy3/Cy5 smFRET traces measured at 100 mM $MgCl_2$ for duplex on (A) quartz and (B) the grating surface; (C-F) smFRET traces of duplex localized in the nanocavity measured at (C) 10 mM, (D) 100 mM, (E) 300 mM, and (F) 1 M $MgCl_2$. The data for quartz substrate was taken with TIRFM, and those for gratings and nanocavities were taken with epi-fluorescence microscope.

of the nanocavities giving rise to this phenomenon. There is also a notable lack of anticorrelated Cy5 intensity fluctuation in those traces showing oscillatory behavior. This will be addressed in the discussion section below.

Power spectral density (PSD) analysis was performed on the smFRET traces exhibiting fluorescence intensity oscillations to identify the characteristic frequencies for each $MgCl_2$ concentration (Figure 3A). After removal of external noise sources (i.e. Brownian, instrument dark current, etc.), PSD analysis showed that oscillation frequency decreased with increasing [$MgCl_2$]. from 0.4 Hz at 100 mM $MgCl_2$ to 0.1 Hz at 1 M $MgCl_2$. At 10 mM $MgCl_2$, there were no apparent intensity oscillations observed (Figure 2C). By extrapolating from the frequencies at higher [$MgCl_2$]., we find that the most likely frequency for 10 mM $MgCl_2$ would be obscured by the instrument dark current noise (~1 Hz) found by PSD analysis of the instrument response post-photobleaching (Supplementary Figure S8).

Fluorescence intensity oscillations report underlying physical phenomena, the identity of which relies on the physical and chemical conditions near the duplex molecule. We know that duplex molecules exhibiting oscillatory behavior are found only at points identified as being part of a nanocavity (Figure 1C). Possible explanations for duplex oscillation in the nanocavities in our case include quenching effects by close proximity to silver, E-field variation resulting in higher localized plasmonic enhancement of Cy3, changes in laser power, and conformational changes in duplex resulting in higher FRET efficiency. The laser power was held constant across all samples at 4.6 mW and so is not responsible for intensity changes between different samples. Silver quenching effects on Cy3/Cy5 have been largely negated by inclusion of the 10 nm SiO_2 spacer layer, which insures the dyes are at least beyond the critical quenching distance for silver (~8 nm) [14]. Variable plasmonic enhancement would rely on a sharp E-field gradient in the vicinity of the Cy3 label. Such gradients are located at the grating–nanocavity interface where the E-field magnitude is highest (Figure 1D). However, duplex molecules localized at the edges of the nanocavities exhibiting highest intensity and, therefore, experiencing highest local E-field displayed no observable periodic oscillations (Supplementary Section 2 and 4). Exclusion of these physical principles as sources of oscillatory behavior leaves conformational changes in the duplex, namely, bending and unbending behavior resulting in increased FRET efficiency between Cy3 and Cy5.

The lack of anticorrelated Cy5 intensity indicative of FRET is attributed to a combination of low FRET efficiency resulting from the dye separation and directional emission of Cy5 wavelengths away from

the detector by surface plasmon-coupled emission (SPCE) [10,25-27]. SPCE occurs when the emitted wavelengths and angular conditions satisfy the dispersion relations for plasmonic gratings in a particular environment, converting normally isotropic emission into directional emission in a narrow angular distribution. The CCD camera window has a 5.1°×10.2° acceptance cone in these experiments (Figure S4) [25]. As a result, any fluorescence emission occurring at angles larger than the objective capture angle will be lost. SPCE significantly reduced emitted photon capture by the detector of Cy5 emission wavelengths. This reduced capture efficiency is illustrated by the study of Holliday Junction molecules (two adjacent arms are labeled with Cy3 and Cy5 molecules while a third arm is tethered to the surface) on two different substrates: quartz substrate (using TIRF), which does not have an angle-dependent emission profile, and silver gratings with embedded nanocavities, which have highly angle-dependent emission and excitation properties (Figure S5). Anticorrelated behavior is apparent for the molecules on quartz, with the on and off states averaging 0.7 and 0.3 FRET efficiency, respectively. The Cy3 channel intensity is 8-10× higher on gratings in epifluorescence mode than the molecules on quartz in TIR mode. Meanwhile, the acceptor emission capture is shown to be severely compromised, corresponding to FRET efficiencies in the on and off states of 0.28 and 0.08, respectively. Assuming that the molecules behave similarly on the two platforms, the energy lost by moving from isotropic (quartz, TIR) to directed (gratings, SPCE) emission can be calculated. The change in FRET on and off states represents a loss of 60% to 75% of acceptor emission capture.

Periodic DNA motion has been observed in the presence of external forces such as a secondary laser, pH modulation, and chemical changes [28-30]. Based on the above observations, the origin, amplitude, and frequency of the oscillatory bending behavior must be strongly *dependent* on [$MgCl_2$]. while *independent* of silver proximity and variation in E-field magnitude. We further posit that the molecules displaying oscillatory behavior should be located deep within the nanocavity. This is supported by the fact that molecules residing on the gratings display no oscillatory behavior (Figure 2B) in the same sample in which nanocavity-bound molecules do oscillate (Figure 2D). Furthermore, the E-field magnitude deep within the nanocavity is much lower than that at the edges and varies by less than 10% of the incident field strength (Figure 1E), which is consistent with our observation that those molecules at the edges of the nanocavities display no oscillatory behavior.

Discussion

The bending of DNA strands shorter than the persistence length (<50 nm or <150 bp) [31] is retarded in ambient conditions due to high entropy costs, though there have been observations to the contrary [32,33]. Further, it is well established that high [Mg^{2+}]. significantly reduces the persistence length due to the screening of electrostatic repulsion between the negatively charged phosphate groups on the DNA backbone [34]. The increased charge screening effect with increasing [Mg^{2+}]., leads to more stable collapsed conformational state of the DNA as is illustrated on the right in Figure 4B. The collapsed conformation pulls the dye pair closer together, which could be viewed in our FRET system as a generally lower initial Cy3 intensity at higher salt concentrations (Figure 3B), the Cy5 emission lost outside the viewable range of the camera due to SPCE as explained above. The collapsing effect of increased salt concentration can also be seen in the overall decay in fluorescence intensity at 300 mM and 1M $MgCl_2$ (Figures 2E and 2F). This decay is inconsistent with the single-step photobleaching observed in Figures 2A-2D. Instead, the higher salt concentration

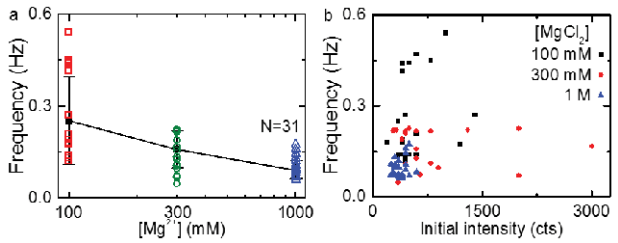

Figure 3: (A) Fluorophore intensity oscillation frequency as a function of Mg^{2+} ion concentration (open points represent frequencies extracted from individual recordings) and (B) Oscillation frequency as a function of $MgCl_2$ concentration and initial fluorophore intensity.

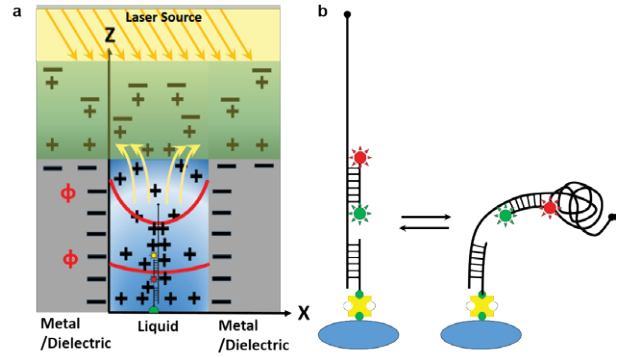

Figure 4: (A) Schematic of the ion concentration distribution within the nanocavity against that in the bulk and the convection induced by the laser source and (B) Bending behavior of duplex in the presence of variable ion flux.

perturbs the duplex molecules deep within the nanocavities, inducing the cyclical bending/unbending behavior as in Figure 2D, but ultimately trends toward a more stable bent or collapsed duplex conformation.

A similar charge screening effect occurs within the negatively charged SiO_2-coated nanocavity; the counterion in the nanocavity should form a double layer with length λ on each wall. Using the classical relation $\lambda = 0.304/\sqrt{I}$, λ is found to be ~5 nm for the lowest ion concentration (10 mM). As the channel dimension (h) approaches $h \sim \lambda$, as in a nanocavity, the double layers start to overlap resulting in ion-selective membranes [35]. However, ion selectivity in nanocavities can occur even for $h>2\lambda$ [36]. An overlapped double layer effect can be seen here, even though the nanocavity dimensions (w=20-200 nm, d=20-100 nm) are much larger than the predicted double layer length. If the negatively charged duplex was located deep within the negatively charged SiO_2 nanocavity, it will lead to the formation of a roughly unipolar solution of Mg^{2+} and other positive ions while negatively charged ions are simultaneously expelled (Figure 4A), an effect similar to ion-selective nanopores [36].

To determine the physics behind the initiation and continuation of the nanocavity based duplex fluctuations, it is necessary to examine the convective and diffusive mechanisms in the nanochannel and examine the possibility of plasmonic heating causing the oscillations. For plasmonic heating, an external E-field produces localized heating when it undergoes focusing in nanocavities, setting up a convective electroosmotic flux known as the thermal end effect [37]. This thermally-induced ion flux can create convective fluxes leading to

disturbances in the concentration profile proportional to the charge inside the nanocavity [38]. However, here as the plasmonic enhanced field focusing is limited to the upper rim of the nanocavity (Figure 1D), thus any associated plasmonic heating will be limited to the surface only. Further, it is well established that diffusive forces dominate over convective forces in plasmonic systems, as illustrated by the associated small dimensionless thermal Péclet number (Pe) of ~10^{-9} when calculated using any standard temperature-based method (details in Supplementary Section SI-6). [38]. Thus, there is negligible increase in temperature near the duplex due to plasmonic heating, failing to melt or denature the duplex deep within the nanocavity. This arrangement is confirmed by the presence of fluorescence from molecules in the nanocavity, which would be rapidly removed if plasmonic heating above the melting temperature (~65°C for the 20-bp duplex region) [39]. occurred near the duplex itself. Further, the diffusive forces relax at the order of μs and, thus, will not contribute to the frequencies observed here.

However, exchanging the thermal velocity flow with an equivalent electroosmotic flow (due to free charges), the field gradient (osmotic pressure) induced convective flow due to plasmonic E-field focusing can be accounted for using an ionic Peclet number. This ionic Pe (2.95×10^{-3}) is relatively higher (details in Supplementary Section SI-6), which indicates increased convective forces, specifically near the rim of the nanocavity where the field focusing is highest (Figure 1D). Thus, we identify the source of the oscillations as an axial ionic gradient flux resulting in a curved ion concentration profile from the increased convective forces similar to that observed in the thermal end effects from external E-field focusing in nanocavities [37]. The ion concentration profile can propagate into the nanocavity, leading to a subsequent Maxwell stress profile near the DNA duplex and providing sufficient osmotic forces to bend the duplex and begin the oscillatory cycle.

We can now assert that the initial oscillation frequencies are determined by the [Mg^{2+}]. and localization of the duplex deep within a nanocavity to form an overlapped double layer and have sufficient E-field magnitude to induce thermally stimulated electroosmotic flow. Due to size and depth variations in the randomly generated nanocavities in this experiment, there is an equally wide variety of E-field magnitudes as well as double layer lengths within the nanocavities, leading to high variation in backbone flexibility, initial intensity, and oscillation frequency in the presence of moderately high bulk [Mg^{2+}] (Figures 2 and 3B). Meanwhile, the 1 M $MgCl_2$ results in sufficient high [Mg^{2+}] concentration to induce stable collapsed conformational state of the duplex regardless of location, which is evidenced by the lower initial fluorescence intensity and oscillation frequency (Figure 3). This is also illustrated through linking the donor intensity with the salt concentration, which shows wide variation due to the random nanocavity dimensions, but overall lower oscillation frequency and frequency variability with increasing salt concentration (Figure 3B). In the presence of high salt concentration, the molecule oscillates, but the oscillation amplitude damps with time in a system resembling an underdamped mass-spring-dashpot system (Figures 2D and 2E). In this case, the DNA is the mass, the electroosmotic flow and [Mg^{2+}]. gradient is the spring, and stabilization by charge screening is the dashpot or damper. This explains the oscillation of the duplex, for the charge screening effect at high [Mg^{2+}]. is reversible and depends on system entropy [34]. The end convective flux of Mg^{2+} will lead to lowering of the positive ions in the cavity leading to duplex straightening [34]. After duplex straightening, there will be excess surface charge inside due to duplex charged backbone. To satisfy this changed electro-neutrality condition inside the nanocavity, it will lead to excess Mg^{2+} ions inside the cavity. These excess positive ions should leading to DNA bending. Thus, the energy necessary to reverse the bending process is supplied by the laser fluence and plasmonic field focusing effect [29]. A more quantitative explanation of these phenomena will require detailed simulation and experimentation with focus on characterizing the nanocavity dimension and length-height aspect ratio to optimize plasmonic field focusing and, thus, concentration gradient.

In summary, we have detailed a preliminary observation of unique oscillatory DNA/RNA duplex bending behavior in a single molecule fluorescence study using an epifluorescence mode microscope setup. The oscillation frequency was found to be governed by the bulk cation concentration, location of the duplex within the nanocavity, and the duplex molecular composition (Figure S9). This study sets the framework for further analysis of complex molecular interactions with the local environment. Characterizing oscillation frequency, amplitude, and damping rate with respect to varying duplex length, nucleotide content, and base-pair matching could provide abundant information for a library of hybrid duplex structures. Monitoring subsequent changes in a given duplex oscillation amplitude and frequency on addition of a ligand or analyte of interest allows tracking of DNA-ligand interactions as well as single nucleotide polymorphisms, leading to a better understanding of those systems and environmental effects on their interactions. Follow-up studies will be performed with greater focus on molecule- and ion-concentration-specific oscillation frequency and damping rates as well as the influence of the nanocavity dimensions on the extent of this behavior.

Acknowledgements

Funding for this work was provided by a grant from the National Science Foundation (Award No. ECCS-1102070).

Author Contributions†

S. B. and A. P. contributed equally to this work. All authors contributed to conception of the experiments, analysis, and interpretation of results. A. P. and D. M. performed primary single molecule experiments. S. B., A. P., B. C., D. M., and C.M.D. analyzed the results. B. C. developed the nanocavity model and simulations. K. G., P. V. C., and S. G. advised on planning and executing the research. All authors discussed the results and contributed to the editing of the manuscript.

Competing Financial Interests

The authors declare that they have no competing interests that stand to benefit financially from the publication of this work or might be perceived to influence the results and discussion in this work.

References

1. Levene MJ, Korlach J, Turner SW, Foquet M, Craighead HG, et al. (2003) Zero-mode waveguides for single-molecule analysis at high concentrations. Science 299: 682-686.
2. Armani AM, Kulkarni RP, Fraser SE, Flagan RC, Vahala KJ (2007) Label-free, single-molecule detection with optical microcavities. Science 317: 783-787.
3. Roy R, Hohng S, Ha T (2008) A practical guide to single-molecule FRET. Nat Methods 5: 507-516.
4. Jain A, Liu R, Ramani B, Arauz E, Ishitsuka Y, et al. (2011) Probing cellular protein complexes using single-molecule pull-down. Nature 473: 484-488.
5. Chu S (1991) Laser manipulation of atoms and particles. Science 253: 861-866.
6. Deniz AA, Dahan M, Grunwell JR, Ha T, Faulhaber AE, et al. (1999) Single-pair fluorescence resonance energy transfer on freely diffusing molecules: observation of Forster distance dependence and subpopulations. Proc Natl Acad Sci 96: 3670-3675.
7. Haustein E, Schwille P (2003) Ultrasensitive investigations of biological

systems by fluorescence correlation spectroscopy. Methods 29: 153-166.

8. Lakowicz JR (2006) Plasmonics in Biology and Plasmon-Controlled Fluorescence. Plasmonics 1: 5-33.
9. Lakowicz JR (2001) Radiative decay engineering: biophysical and biomedical applications. Anal Biochem 298: 1-24.
10. Lakowicz JR (2005) Radiative decay engineering 5: metal-enhanced fluorescence and plasmon emission. Anal Biochem 337: 171-194.
11. Gramotnev DK, Bozhevolnyi SI (2010) Plasmonics beyond the diffraction limit. Nat Photon 4: 83-89.
12. Homola J, Yee SS, Gauglitz G (1999) Surface plasmon resonance sensors: review. Sensors and Actuators B: Chemical 54: 3-15.
13. Homola J1 (2008) Surface plasmon resonance sensors for detection of chemical and biological species. Chem Rev 108: 462-493.
14. Bhatnagar K, Pathak A, Menke D, Cornish PV, Gangopadhyay K, et al. (2012) Fluorescence enhancement from nano-gap embedded plasmonic gratings by a novel fabrication technique with HD-DVD. Nanotechnology 23: 49520.
15. Liu Z, Boltasseva A, Pedersen RH, Bakker R, Kildishev AV, et al. (2008) Plasmonic nanoantenna arrays for the visible. Metamaterials 2: 45-51.
16. Ni X, Emani NK, Kildishev AV, Boltasseva A, Shalaev VM (2012) Broadband light bending with plasmonic nanoantennas. Science 335: 427.
17. Liu Z, Steele JM, Srituravanich W, Pikus Y, Sun C, et al. (2005) Focusing surface plasmons with a plasmonic lens. Nano Lett 5: 1726-1729.
18. Ropers C, Neacsu CC, Elsaesser T, Albrecht M, Raschke MB, et al. (2007) Grating-coupling of surface plasmons onto metallic tips: a nanoconfined light source. Nano Lett 7: 2784-2788.
19. Ebbesen TW, Lezec HJ, Ghaemi HF, Thio T, Wolff PA (1998) Extraordinary optical transmission through sub-wavelength hole arrays. Nature 39: 667-669.
20. Lévêque G, Martin OJ (2006) Optical interactions in a plasmonic particle coupled to a metallic film. Opt Express 14: 9971-9981.
21. Mock JJ, Hill RT, Degiron A, Zauscher S, Chilkoti A, et al. (2008) Distance-dependent plasmon resonant coupling between a gold nanoparticle and gold film. Nano Lett 8: 2245-2252.
22. Mock JJ, Hill RT, Tsai YJ, Chilkoti A, Smith DR (2012) Probing dynamically tunable localized surface plasmon resonances of film-coupled nanoparticles by evanescent wave excitation. Nano Lett 12: 1757-1764.
23. Shannon CE (1949) Communication in the Presence of Noise. Proceedings of the IRE 37: 10-12.
24. Ha T, Rasnik I, Cheng W, Babcock HP, Gauss GH, et al. (2002) Initiation and re-initiation of DNA unwinding by the Escherichia coli Rep helicase. Nature 419: 638-641.
25. Xiao M, Selvin PR (2001) Quantum yields of luminescent lanthanide chelates and far-red dyes measured by resonance energy transfer. J Am Chem Soc 123: 7067-7073.
26. Gryczynski I, Malicka J, Gryczynski Z, Lakowicz JR (2004) Radiative decay engineering 4. Experimental studies of surface plasmon-coupled directional emission. Anal Biochem 324: 170-182.
27. Darr CM, Korampally V, Chen B, Gangopadhyay K, Gangopadhyay S (2014) Plasmonic-enhanced conjugated polymer fluorescence chemosensor for trace nitroaromatic vapor. Sensors and Actuators B: Chemical 202: 1088-1096.
28. Prescott B, Steinmetz W, Thomas GJ Jr (1984) Characterization of DNA structures by laser Raman spectroscopy. Biopolymers 23: 235-256.
29. Mayama H, Nomura SM, Oana H, Yoshikawa K (2000) Self-oscillating polymer chain. Chemical Physics Letters 330: 361-367.
30. Liedl T, Simmel FC (2005) Switching the conformation of a DNA molecule with a chemical oscillator. Nano Lett 5: 1894-1898.
31. Baumann CG, Smith SB, Bloomfield VA, Bustamante C (1997) Ionic effects on the elasticity of single DNA molecules. Proc Natl Acad Sci U S A 94: 6185-6190.
32. Richmond TJ, Davey CA (2003) The structure of DNA in the nucleosome core. Nature 423: 145-150.
33. Wong OK, Guthold M, Erie DA, Gelles J (2008) Interconvertible lac repressor-DNA loops revealed by single-molecule experiments. PLoS Biol 6: e232.
34. Rouzina I, Bloomfield VA (1998) DNA bending by small, mobile multivalent cations. Biophys J 74: 3152-3164.
35. Wang M, Kang Q, Ben-Naim E (2010) Modeling of electrokinetic transport in silica nanofluidic channels. Anal Chim Acta 664: 158-164.
36. Karnik R, Fan R, Yue M, Li D, Yang P, et al. (2005) Electrostatic control of ions and molecules in nanofluidic transistors. Nano Lett 5: 943-948.
37. Xuan X, Sinton D, Li D (2004) Thermal end effects on electroosmotic flow in a capillary. International Journal of Heat and Mass Transfer 47: 3145-3157.
38. Donner JS, Baffou G, McCloskey D, Quidant R (2011) Plasmon-assisted optofluidics. ACS Nano 5: 5457-5462.
39. Sugimoto N, Nakano S, Katoh M, Matsumura A, Nakamuta H, et al. (1995) Thermodynamic parameters to predict stability of RNA/DNA hybrid duplexes. Biochemistry 34: 11211-11216.